Title	Cyclic plasticity of welded P91 material for simple and complex power plant connections
Author(s)	Li, Ming; Barrett, Richard A.; Scully, Stephen; Harrison, Noel M.; Leen, Sean B.; O'Donoghue, Padraic E.
Publication Date	2016-02-10
Publication Information	Li, Ming, Barrett, Richard A., Scully, Stephen, Harrison, Noel M., Leen, Sean B., & O'Donoghue, Padraic E. (2016). Cyclic plasticity of welded P91 material for simple and complex power plant connections. International Journal of Fatigue, 87, 391-404. doi: https://doi.org/10.1016/j.ijfatigue.2016.02.005
Publisher	Elsevier
Link to publisher's version	https://doi.org/10.1016/j.ijfatigue.2016.02.005
Item record	http://hdl.handle.net/10379/15654
DOI	http://dx.doi.org/10.1016/j.ijfatigue.2016.02.005

Cyclic plasticity of welded P91 material for simple and complex power plant connections

Ming Li[1], Richard A. Barrett[1,2,*], Stephen Scully[3], Noel M. Harrison[1], Sean B. Leen[1,2,†], Padraic E. O'Donoghue[2,4,†]

[1]*Mechanical Engineering, College of Engineering and Informatics, NUI Galway, Ireland*
[2]*Ryan Institute for Environmental, Marine and Energy Research, NUI Galway, Ireland*
[3]*ESB Energy International, Little Island, Cork, Ireland*
[4]*Civil Engineering, College of Engineering and Informatics, NUI Galway, Ireland*

Abstract: This paper is concerned with the cyclic plasticity modelling of welded, ex-service P91 material. A multi-material model is developed for high temperature cyclic plasticity, including the effects of the three different material zones in the vicinity of the weld: parent metal, weld metal and heat-affected zone. The cyclic plasticity behaviour of the three zones is identified from previously-published high temperature, low cycle fatigue experimental tests on uniaxial parent metal, weld metal and cross-weld specimens on ex-service P91 material. The heat-affected zone is shown to be significantly softer than the parent and weld metals and to act as a focus for concentration of plastic strain, leading to significantly inhomogeneous distributions of stress and strain in the weldment. The multi-material cyclic plasticity model is applied, via a three-dimensional finite element model, to a welded T-piece header-branch connection, to predict the effects of cyclic internal pressure and small amplitude thermal fluctuations.

Keywords: P91 steel, cyclic plasticity, heat affected zone, power plant, welded connections, thermo-mechanical fatigue.

1. Introduction

The key strategic goal for next generation power plant operation is to significantly increase overall plant efficiency and reduce emissions via increased steam temperatures and pressures (i.e. ultra-supercritical plant operation), whilst operating under flexible conditions to accommodate renewable sources of energy. Safety-critical components such as welded header units (typically manufactured from 9-12Cr steels), will therefore be subjected to (i) more severe thermo-mechanical fatigue (TMF), due to increased thermal gradients imparted on heavy wall components during start-up (attemperation) cycles [1] and (ii) more severe creep-fatigue (CF) loading due to increased steam temperatures and pressures. As welded connections are well known to be 'hot-spots' for premature failure, the key to successful flexible plant operation at higher temperatures and pressures is primarily related to suppression of the CF mechanisms of microstructural degradation and deformation in welded connections.

For base-load operation, the performance of 9-12Cr welded connections in high temperature power plant components is typically dominated by creep mechanisms of deformation. However, as power generation becomes more flexible, such welded connections will become more susceptible to CF deformation, resulting in exacerbated microstructural degradation and

[*]Corresponding Author
Email: richard.barrett@nuigalway.ie
Tel: +353 91 492792
Fax: +353 91 563991
[†] Joint Senior Author

hence, reduced component life. For example, the addition of TMF deformation leads to enhanced coarsening of the microstructure, including martensitic lath widening [2,3] and plastic-strain induced precipitate coarsening [4], resulting in decreased creep strength and reduced CF life. Thus, the severe operational conditions which next generation power plants must endure [1,5] will most likely lead to CF and TMF weldment failures. It is known that these failures commonly occur within the heat affected zone (HAZ) of welded connections (Type IV cracking region), as illustrated in Figure 1, for premature failure of a T-piece connection, following high temperature, flexible operation. For 9-12Cr steels, Type IV cracking is due to heterogeneities in the microstructure, i.e. the hierarchical microstructure of 9-12Cr steels is replaced with coarse (CG-HAZ) and fine-grained (FG-HAZ) structures of reduced creep resistance following welding [6]. In particular, the inter-critical HAZ (IC-HAZ) has been identified as the region of lowest hardness in a welded joint [7], and the primary location of failure in welded 9-12Cr steel connections [6]. Thus, there exists a requirement to be able to predict CF failures in such components using numerical methods.

The long-term, creep behaviour of welded pressurised steam connections has received significant attention, e.g. see Takahashi and Tabuchi [8] and Tanner *et al.* [9], for example. Hyde and co-workers have developed creep damage mechanics constitutive models for a range of materials [10], including welded CrMoV steels [11-13], P91 and P92 parent material (PM) [14], weld material (WM) and HAZ [14-16]. Furthermore, novel methods for identification of the creep constitutive parameters of the HAZ have been developed by Hyde *et al.* [11,15]. The identified multi-material creep parameters have been applied to multi-axial finite element (FE) models of welded pipes [13] and T-joint connections [18]. This has contributed to the understanding of Type IV cracking in such creep applications. Hayhurst and co-workers [19] have presented continuum damage mechanics models of mechanisms-based creep of ferritic CrMoV steels, including creep cavitation and softening due to carbide coarsening. This approach was implemented in FE models including CG-HAZ, FG-HAZ and IC-HAZ, as well as PM and WM, for pressurised CrMoV welded pipes [20].

A number of authors have presented experimental results on the creep (including Type IV cracking), CF, low cycle fatigue (LCF) and TMF behaviour of P91 welded materials and simple welded joints [21-28]. Some work had been carried out by Fournier and co-workers [29], which emphasizes that creep-fatigue type loading will be caused by the repeated start-stop intermittent operation cycle. Other recent work has also focused on accommodating these experimental results into numerical models focused on TMF and creep-fatigue of power plant pipes and branch header connections [1,5], but without explicitly considering the multi-material cyclic plasticity of welded joints behaviour for high temperatures and LCF. Okrajni *et al.* [30] introduced the thermal-mechanical modeling of P91 with complex power plant geometries, only assuming the power plant component as a monolithic structure. Many critical power plant components are fabricated with welded joints, and as such, contain microstructure inhomogeneity. The resulting local mechanical property variation across the joint should be accounted for when predicting fatigue behaviour, by experimentally characterising the behaviour of the individual three distinct zones (PM, HAZ and WM) . Shankar *et al*. [25,26], reported that stress response of welded joints is similar with PM. Yang et al., [28] further investigated and made comparisons about the fatigue life between PM and welded joints specimens. Almost all of the investigations so far have focussed on PM and welded joints, without considering the mechanical response for each material within the welded joints, based on fatigue tests of welded P91 joints. A cycle-by-cycle FE method of fatigue tests was employed to predict the number of cycles to failure for bi-materials, including WM and PM only [31,32]; however, this work did not explicitly model the HAZ, which has a different microstructure and, therefore, associated fatigue and plasticity

characteristics. A number of cyclic plasticity models have been applied to 9-12Cr steels, e.g. the two-layer viscoplasticity model of Farragher *et al.* [33], which was used to characterize the cyclic behaviour of PM, WM, HAZ, and welded joints (CW) for finite element modelling; the latter work did not study stress-strain evolution of the welded joints, which is critical to investigate the mechanism of HAZ cracking. Saad *et al.*[34] and Lee *et al.* [35] proposed modeling of P91 for TMF, only concentrating on the parameter identification process for PM constitutive models which are extracted from the experimental data and without referring to modelling of the welded joints under thermo-mechanical fatigue conditions.

As discussed in [36,37], strain-rate effects are not significant for 9-12Cr steels at temperatures of 500 °C or lower. The need to develop cyclic plasticity constitutive models to simulate P91 steels under more realistic strain-rates was recently addressed by Barrett *et al.* [38], wherein an improved unified cyclic viscoplastic constitutive model for strain-rate sensitivity in high temperature fatigue was developed. Barrett *et al.* [36] further extended this model to incorporate microstructural parameters for martensitic lath width, dislocation density and precipitate spacing, at the macro-scale, as part of a multi-scale modelling methodology. The requirement for a multi-scale modelling methodology is dictated by the complex nature of 9-12Cr steel microstructures and the necessity to be able to predict the effects of key strengthening mechanisms, such as precipitates for example [36,38,39].

The first part of this paper presents material parameter identification and development of a multi-material model for high temperature cyclic plasticity of the three different material zones in the weld region, as well as investigation of the evolution of the stress-strain distribution in uniaxial P91 weld specimens. The second part of the paper presents a three-dimensional FE model of a P91 welded header-branch T-piece (see Figure 2), for cyclic plasticity analyses of the multi-material connection, using the newly determined constitutive parameters and for combined thermal-mechanical loading histories. The objective is to explore the evolution of cyclic plasticity in the three different weldment zones under different loading conditions, with a view to gaining some insight into possible failure locations and modes of deformation. Some comparison is made between the predicted behavior and reported industry findings of damage for the T-piece.

2. Experimental program

2.1. Test specimen extraction

In order to identify the cyclic plasticity constitutive parameters for different weld-related material zones (PM, WM, HAZ), the results of a recent HTLCF testing programme are analysed. As described in Farragher *et al.* [33], PM, WM, and cross weld (CW) test specimens were extracted from a specially fabricated girth weld in an ex-service P91 header. Thus, the weldment analysed in this study is representative of a repair weldment. Figure 3 illustrates the location where the HTLCF test specimens were extracted from the ex-service header unit. Note that the CW specimen has PM at one end, WM at the other end and HAZ in the middle. The P91 header used for this weldment was an ex-service header with about 35,000 hours' service, under subcritical loading conditions. Further details of the preparation and testing of these HTLCF test specimens as well as the material properties and composition of the parent P91 and weld electrode have been previously reported [33].

2.2. HTLCF behaviour of welded P91 steel

Uniaxial material testing on preheated specimens was conducted on the HTLCF test rig at NUI Galway (Figure 4). Figure 5 shows a comparison of the measured stress-strain hysteresis loops and the cyclic evolution of maximum stress for the three different specimens (PM, WM and CW) subjected to a strain-controlled triangular waveform for a strain-range of 1.0 % at a strain rate of 0.033 %/s and a temperature of 500 ˚C. As can be seen from Figure 5a, the CW has a similar cyclic response to the PM specimen for the first cycle, which suggests that the initial mechanical behavior of the HAZ is similar to that of the PM. In addition, it is clear that the WM exhibits the highest cyclic strength when compared to that of the other two materials, as expected for an over-matched weldment. It is also clear from Figure 5b that all three specimen types exhibit cyclic softening, which is characteristic of high temperature cyclic deformation of P91. The WM specimen shows the highest rate of cyclic softening; the rate of softening of the CW specimens is a little less severe than the PM specimen. The CW specimen exhibits the shortest fatigue life, with the PM specimen exhibiting the longest, almost 2.5 times that of the CW specimen.

3. Cyclic plasticity constitutive model

The cyclic plasticity model uses J_2 flow theory with combined non-linear kinematic and isotropic hardening to define the constitutive behaviour of the material. The increment in stress is defined using multi-axial Hooke's law:

$$\dot{\boldsymbol{\sigma}} = \mathbf{C}_e : \dot{\boldsymbol{\varepsilon}}_e = \mathbf{C}_e : \left(\dot{\boldsymbol{\varepsilon}} - \dot{\boldsymbol{\varepsilon}}_p\right) \tag{1}$$

where $\dot{\boldsymbol{\varepsilon}}_e$, $\dot{\boldsymbol{\varepsilon}}$ and $\dot{\boldsymbol{\varepsilon}}_p$ are the elastic, total and plastic strain-rate tensors, respectively, and $\mathbf{C}_e$ is the fourth-order tensor of elastic moduli, defined in terms of Young's modulus, E, and Poisson's ratio, v. As discussed in [36,37], significant strain-rate effects are observed at temperatures of greater than 500 °C in the ex-service P91 steel tested here. This permits a simplification in terms of modelling, viz. time-independent cyclic plasticity can be employed, as opposed to a more complex cyclic viscoplasticity model [**Error! Reference source not found.**34,38,40]. Thus, the plastic strain-rate is defined using the following equation set:

$$\dot{\boldsymbol{\varepsilon}}_p = \dot{p}\frac{\partial f}{\partial \boldsymbol{\sigma}} \tag{2}$$

$$\dot{p} = \frac{\dfrac{\partial f}{\partial \boldsymbol{\sigma}} : \mathbf{C}_e \dot{\boldsymbol{\varepsilon}}}{\dfrac{\partial f}{\partial \boldsymbol{\sigma}} : \mathbf{C}_e \dfrac{\partial f}{\partial \boldsymbol{\sigma}} + \boldsymbol{\Phi} : \dfrac{\partial f}{\partial \boldsymbol{\sigma}} + \Omega} \tag{3}$$

$$f = \left(\frac{3}{2}\left(\boldsymbol{\sigma}' - \mathbf{x}'\right) : \left(\boldsymbol{\sigma}' - \mathbf{x}'\right)\right)^{\frac{1}{2}} - R - k = 0 \tag{4}$$

where $\dot{p}$ is the accumulated effective plastic strain-rate, f is the yield function, $\boldsymbol{\Phi}$ is a non-linear kinematic hardening function, Ω is an isotropic hardening term, $\mathbf{x}$ is kinematic back-stress, R is isotropic stress, k is cyclic yield stress and $\boldsymbol{\sigma}'$ and $\mathbf{x}'$ are the deviatoric stress and back-stress tensors, respectively. The kinematic back-stress term is used to represent the Bauschinger effect. This is important for accurate representation of the cyclic stress-strain hysteresis loops, which in turn is critical for accurate life prediction. In the present work, two back-stress terms are defined within a Ziegler non-linear kinematic hardening model [41] to describe the initial and later strain hardening regions, as follows:

$$\dot{\mathbf{x}}_i = \frac{C_i}{(k+R)}(\boldsymbol{\sigma}-\mathbf{x})\dot{p} - \gamma_i \mathbf{x}_i \dot{p} \tag{5}$$

$$\dot{\mathbf{x}} = \dot{\mathbf{x}}_1 + \dot{\mathbf{x}}_2 \tag{6}$$

where C_i is the kinematic hardening modulus and γ_i is the rate of decay.

Due to a loss of the low-angle boundary microstructure, i.e. plastic-strain induced recovery via low-angle boundary dislocation annihilation [2,3], P91 steels undergo cyclic softening. This is represented in the cyclic plasticity model via the isotropic hardening model of Chaboche [42,43]:

$$\dot{R} = b(Q-R) \tag{7}$$

where Q is the saturation value of the isotropic softening stress and b controls the rate of decay leading to saturation. A negative value of Q allows modelling of the cyclic softening phenomena in the material at a continuum level [34].

4. Parameter identification and calibration

4.1. Identification of the PM and WM material parameters

The constitutive parameter identification process for the PM and WM follows that described by Hyde *et al.* [44] and Barrett *et al.* [45], based on the cyclic plasticity test data from the uniaxial HTLCF tests on PM and WM specimens. The required material parameters are separated into two groups: (i) elastic parameters and (ii) the cyclic plasticity material parameters. The elastic material parameters are Young's modulus, E, and Poisson's ratio, v, which are identified from the monotonic (1st cycle) test data. The cyclic plasticity parameters of cyclic yield stress, k, non-linear kinematic hardening constants (C_i, γ_i) and isotropic softening parameters (Q, b) are determined using a step-by-step procedure, as described here.

Firstly, the isotropic softening constants (Q, b) are identified via consideration of the cyclic softening curves. The isotropic stress is identified from the experimental data by plotting $R = \sigma_{\max} - \sigma_{0,\max}$ against p (the accumulated equivalent plastic-strain $p = \text{abs}(2N\Delta\varepsilon_p)$). Due to continued cyclic softening in 9-12Cr steels, the value of Q is taken to be the isotropic stress, R, just prior to the onset of failure, as highlighted in Figure 6. The parameter b, which describes the rate of decay of R, is then adjusted to give the best fit to the experimental data, as shown in Figure 6. The cyclic yield stress value is then identified following the approach described by Lemaitre and Chaboche [46], based on plotting plastic-strain versus stress and estimating the length of the vertical portion of the curve when the material response becomes stabilized, as illustrated in Figure 7. Finally, the non-linear kinematic hardening parameters (C_i, γ_i) are determined using the approach developed by Zhan [47]. Under uniaxial loading conditions, Equation (4) is rewritten to define the stress, σ, as:

$$\sigma = x + (R+k)\text{sgn}(\sigma - x) \tag{8}$$

Integrating the uniaxial form of Equations (5) and (6) gives the kinematic back-stress, x, and isotropic softening stress, R, as:

$$x = x_1 + x_2 = \frac{C_1}{\gamma_1}\left(1 - e^{-\gamma_1 \varepsilon_p}\right) + \frac{C_2}{\gamma_2}\left(1 - e^{-\gamma_2 \varepsilon_p}\right) \tag{9}$$

$$R = Q(1 - e^{-bp}) \tag{10}$$

For the later stages of kinematic hardening, the initial back-stress, x_1, will have a constant (maximum) value of C_1/γ_1. Thus, taking the natural logarithm of the derivative of Equation (9) with respect to the plastic strain, ε_p, gives:

$$\ln\left(\frac{\partial\sigma}{\partial\varepsilon_p} - Qbe^{-bp}\right) = \ln(C_2) - \gamma_2\varepsilon_p \tag{11}$$

In the Equation (11), the term $\partial\sigma/\partial\varepsilon_p$ is evaluated using a process involving a Ramberg-Osgood smoothing function [47] and the kinematic back-stress constants, C_2 and γ_2 are identified from the intercept and slope, respectively, of the plot of $\ln\left(\partial\sigma/\partial\varepsilon_p - Qbe^{-bp}\right)$ versus the plastic strain, ε_p, as presented in Figure 8a for the WM specimens. The constants for the first kinematic back-stress term, viz. C_1 and γ_1, are identified by plotting $\ln\left(\partial\sigma/\partial\varepsilon_p - Qbe^{-bp} - \partial x_2/\partial\varepsilon_p\right)$ versus the plastic strain, ε_p, as presented in Figure 8b. the same identification process was applied to the PM specimen test data, to identify the corresponding parameters for the PM. The identified set of cyclic plasticity parameters for the PM and WM are presented in Table 1.

This identification process is effected via uniaxial implementation of the equations above, implemented within a stand-alone computer program, for a strain-rate of 0.033 %/s and an applied strain-range of ±0.5 %. Figure 9a illustrates the agreement between the calibrated model and the experimental data, for the initial and half-life cycle of PM at 500 °C. For this study, N_f corresponds to the number of cycles to fracture of the test specimen. The model is applied to simulate $N_f/2$ cycles because the fracture mechanisms required to capture the final stage of failure are not the focus of this work. The comparison of model and measured softening behavior of the PM is shown in Figure 9b. The corresponding comparisons for the WM test specimen are presented in Figure 10a and Figure 10b.

4.2. Determination of the HAZ material parameters

Identification of the corresponding HAZ parameters requires iterative computations using a finite element model of the CW test specimen (cylindrical) gage length, with the three separate material zones (PM, WM, HAZ) modelled. The finite element code employed here is the general-purpose, non-linear code, Abaqus™. The built-in nonlinear kinematic-isotropic hardening model in Abaqus is used for the CW model. Design of the FE mesh used for the CW test specimen is based on the results of mesh convergence studies, with particular emphasis on the weld zone interfaces, where discontinuities are expected. Hence, the final mesh is designed to give detailed mesh refinement at the interfaces of the materials and HAZ, as shown in Figure 11. A totally number of 1140 quadratic quadrilateral elements of type CAX8R has been used in the three-material model. The smallest size elements at HAZ region is about 0.09 mm. The elastic modulus of the HAZ is obtained using an in-series three spring model, which is used for representing the multi-material zones, as follows:

$$\frac{x_{CW}}{k_{CW}} = \frac{x_{PM}}{k_{PM}} + \frac{x_{HAZ}}{k_{HAZ}} + \frac{x_{WM}}{k_{WM}} \tag{12}$$

where k_{CW}; k_{BM}; k_{HAZ}; k_{WM} are the Young's moduli identified from experimental data and x_{CW}; x_{BM}; x_{HAZ}; x_{WM} are the lengths of each material within the CW specimen. Poisson's ratio for

the HAZ is assumed to be 0.3. Based on the similarity of the CW and PM stress-strain curves, (Figure 5), the initial values of the kinematic back-stress parameters for the HAZ are assumed to equal those of the PM and the yield stress was lower than the corresponding value of PM based on the hardness test from Farragher *et al.* [33].The remaining HAZ plastic parameters were fitted to the experimental CW stress-strain data through the strain-control test response of three-material model for the first cycle and the half-life cycle (Figure 12).

The complete set of identified cyclic plasticity parameters for the three-material zones is given in Table 1. The degree of cyclic softening (Q) and decay rate (b) in the HAZ (-80 MPa, 0.1, respectively) is found to be significantly less than that in the WM (-150 MPa, 0.6, respectively); which is reflected in the cyclic softening test data in Figure 5b. A comparison of the predicted and experimentally-measured stress-strain CW response for the calibration strain-range of ±0.5 % and strain-rate of 0.033 %/s are presented in Figure 12. The corresponding comparisons for the ±0.3 % and ±0.4 % strain ranges showed a similar quality of correlation.

5. Results and Discussion

5.1. Cyclic plasticity analyses of a uniaxial welded joint

Figure 13 to Figure 15 present the cyclic evolutions of von Mises stress, axial plastic strain and equivalent accumulated plastic-strain in the gauge section of the CW specimen, for a nominal applied strain-range of 1.0 % and nominal strain-rate of 0.0333 %/s. These results illustrate (i) a significant degree of inhomogeneity across all three zones and (ii) significant evolutions in the distributions of these variables due to the differences in softening parameters across the three zones.

As is evident from Figure 13, there is a significant inhomogeneity (~150 MPa) of von Mises stress across the CW specimen zones for $N = 1$, with peak and trough values either side of the WM-HAZ interface. The peak von Mises stress is predicted in the WM. With continued cycling to the half-life (495 cycles), the stress relaxes significantly in the WM and the WM-HAZ discontinuity of von Mises stress-range decreases to approximately 100 MPa. Concomitantly, a discontinuity develops at the HAZ-PM interface, with peak value on the PM side.

Referring to Figure 14, there is an initial concentration of axial plastic strain at the HAZ-PM interface, with a peak in the HAZ. This is attributed to the lower initial yield stress of the HAZ (Table 1). Under continued cycling, the HAZ continues to soften, giving an increased extent of concentration of axial plastic strain in the HAZ, particularly at the HAZ-PM interface. For the CW tests, to which this analysis corresponds, this prediction also corresponds to the location of Type IV cracking in the test, i.e. at the HAZ-PM interface [33] as illustrated in Figure 14. Furthermore, at the half-life, there are regions of concentrated axial plastic strain of up to 4 % in the HAZ, outer surface and central axis. This represents a strain concentration factor of ~8, given that the maximum applied strain is 0.5 %. This illustrates the ability of the calibrated model to predict the correct location of failure and also highlights the necessity to be able to predict the constitutive behaviour in a welded connection under cyclic deformation.

It is also of interest to investigate the equivalent accumulated plastic-strain, as presented in Figure 15, which has been proposed by a number of authors, e.g. Sweeney *et al.* [48], as a fatigue indicator parameter for crack initiation prediction. The predicted equivalent

accumulated plastic-strain displays a concentrated region of significant magnitude at the half-life, focused on the HAZ-PM interface.

5.2. Branch Header T-Joint

The calibrated material model is applied to the case of a T-joint welded connection (Figure 2) in a branched header unit. The geometry is obtained from a combined cycle gas turbine plant header unit and is used to investigate the cyclic plasticity behavior of in-service welds. This T-joint failed prematurely, after less than 10,000 hours of high temperature, flexible service. The branch has two weld sections, one connecting the weldolet to the header and the other connecting the weldolet to the branch. Key geometrical information for the T-joint is presented in Table 2. In order to investigate an envelope of possible cyclic plasticity responses for the T-piece, within the constraints of the identified PM-WM-HAZ material model data, different combinations of internal pressure, system constraint and thermal cycle conditions are investigated, as tabulated in Table 3. Two internal pressures are considered: (i) a typical operating (subcritical) pressure of 17 MPa and (ii) a significantly increased, USC operating pressure of 25 MPa. Two different thermal conditions are considered: (i) an isothermal condition (500 $^{\circ}$C) and (ii) a small fluctuation of temperature between 480 $^{\circ}$C and 520 $^{\circ}$C, over which range of temperature it is not unreasonable to assume that the 500 $^{\circ}$C material constants are unchanged. Finally, two different system constraint conditions are considered: (i) closed-end condition for the end cap, and (ii) extreme system constraint, leading to constrained end cap in the axial direction, as illustrated in Figure 16.

A mesh sensitivity study of the T-piece was conducted using converged elastic-plastic stresses to determine suitable mesh resolution in the weldment region. Five meshes were used with varying density from coarser to finer mesh densities. The mesh using 61,495 elements (mesh used here) provided the same result as the most refined mesh considered, which had 128,748 elements. Figure 17 shows detail of the mesh refinement for the converged FE model used in these simulations. This mesh used a combination of 61,495 brick and tetrahedral elements, consisting of 31,854 brick elements of type C3D8, 2400 linear brick elements of type C3D8R and 27,241 quadratic tetrahedral elements of type C3D10. Tetrahedral elements were used in the fillet weld, because the geometry was too complex to successfully implement brick element meshing. The smallest element sizes in the fillet and branch HAZ regions are about 1.02 mm and 0.5 mm, respectively. The use of brick elements is considered important for the HAZ regions, in particular, as shown in Figure 17.

A key objective of this T-piece study was to examine the effects of the inhomogeneous cyclic plasticity, especially softening of the PM, WM and HAZ zones, on the T-piece response. Thus, this evolution of constitutive behavior could be expected to give rise to elastic shakedown, plastic shakedown or ratcheting within the complex multi-axial geometry of a T-joint. Of the eight different T-joint analyses studied, seven cases led to plastic deformation in the HAZ regions, followed by elastic shakedown. It is also of interest to investigate the possible failure modes and locations indicated by these multi-material analyses, albeit with somewhat limited assumptions. Only the case of high internal pressure, 25 MPa, with fluctuating temperature and extreme system constraint, gave cyclic plasticity, more specifically ratchetting.

5.2.1. Case 1: Isothermal, normal operating pressure with closed ends

Isothermal conditions were specified in this first model, in order to assess the predicted plastic deformation behavior and the predicted failure locations.

Contour plots of the results from this simulation are presented in Figure 18 to Figure 20. In each contour plot, the outer wall is shown in the left plot and the inner wall is shown in the right plot. There are two regions with concentrations of maximum principal stresses; the inner crotch, labelled A, and the outer saddle position, labelled B in Figure 18. The directions of the principal stresses at these sites are shown by the vector plots in the inset images of Figure 18. These illustrate the directions of the maximum (tensile) principal stresses. Of specific interest here is the concentration of tensile stress at the saddle HAZ location (labelled B) and direction of principal stresses. This location is the observed location of premature cracking in a T-piece of similar geometry (see inset in Figure 19).

For this same location (B), with the tensile principal stress concentration in Figure 18, the contour plot of equivalent plastic strain in Figure 19 also shows a HAZ concentration, associated with the initial plastic deformation. As cyclic softening in 9Cr steels is primarily due to plastic strain induced recovery, the low plastic strain-range for an applied internal pressure of 17 MPa (as illustrated in Figure 20) is expected to result in negligible softening. Elastic shakedown has occurred at this stage and hence no further cycles are simulated. Figure 20 shows the effect of applied pressure on the evolution of $\sigma_{11} - \varepsilon_{11}$ response at this HAZ location. A small initial plastic strain of 0.005% is predicted at the end of the first loading cycle. Also shown in Figure 20 is the response for an internal pressure of 25 MPa, resulting in initial plasticity of 0.05%, also with elastic shakedown. This result highlights potential issues with operating power plants at higher pressures (i.e. corresponding to USC plant operation). Coupled with typically higher USC plant operating temperatures, higher pressures will result in higher plastic strains and hence, increased risk of premature component failure.

5.2.2. Case 2: Extreme USC TMF operating conditions

The second case of specific interest here corresponds to a USC cyclic pressure of 25 MPa with an in-phase small cyclic temperature fluctuation from 480 °C to 520 °C, with a fixed end constraint on the branch end. In this work, all the constants were specified at the mean temperature of 500 °C. This particular model configuration can be regarded as an extreme load condition within operational parameters currently considered possible. The resulting distribution of predicted equivalent accumulated plastic strain after 51 cycles is shown in Figure 21. There are clear concentrations of equivalent accumulated plastic strain of about 0.3% in the weldolet HAZ at the inner crotch position (i.e. at location A). The effect of applied pressure on the evolution of $\sigma_{11} - \varepsilon_{11}$ (hoop) response accompanying the temperature variation is shown in Figure 22. This component will deform plastically when the stress exceeds 120 MPa, the yield stress of the HAZ. Initially, a plastic strain of 0.024% is predicted, followed by a clear ratcheting effect, due to the fluctuating thermally-induced strains. The ratcheting strain in this direction gradually decreases as the cycles continue, indicating a tendency towards plastic shakedown. However it does not go to zero, as illustrated in Figure 23. Obvious softening effects can be seen, whereby the σ_{11} stress component in this HAZ hotspot of the T-joint deceases continuously from 243 MPa at the 1st cycle to 184 MPa at the 51st cycle. The total axial plastic strain is 0.06 % after 51 cycles. The ratcheting response was found at both the weldolet-header and weldolet-branch HAZ regions (Figure 21). It also can be observed that the equivalent ratcheting strain is dominated by the σ_{11} stress component. For this ratcheting behaviour, the number of ratcheting cycles to failure, N_f, may be estimated by the following equation:

$$\sum_{i=1}^{N_f} \Delta\varepsilon_r = \varepsilon_f^* \tag{13}$$

In the above equation, $\Delta\varepsilon_r$ is an equivalent ratchet strain and can be calculated as $\Delta\varepsilon_r = \sqrt{\frac{2}{3}\Delta\varepsilon_{ij}^r \Delta\varepsilon_{ij}^r}$, $\Delta\varepsilon_{ij}^r$ are the ratcheting strain components of each cycle and ε_f^* refers to the multiaxial failure strain. The void growth model proposed by Rice and Tracey is adopted here as a method to describe the triaxiality effect on multiaxial failure strain, which is presented as follows [49]:

$$\frac{\varepsilon_f^*}{\varepsilon_f} = \frac{0.521}{\sinh\left(\frac{3}{2}\frac{\sigma_m}{\sigma_{eq}}\right)} \tag{14}$$

where ε_f is the uniaxial failure strain and the triaxiality is the ratio of σ_m to σ_{eq}. Figure 24 shows the predicted evolutions of triaxiality response at the hotspot of weldolet-header HAZ, with the following equation used here to obtain the average value of triaxiality:

$$\left(\frac{\sigma_m}{\sigma_{eq}}\right)_{av} = \frac{1}{N_T}\int_0^{N_T} \frac{\sigma_m}{\sigma_{eq}} dN \tag{15}$$

where N_T is the total number of cycles. Thus, the average calculated triaxiality value is approximately 0.5672. The failure strain of a uniaxial P91 CW test specimen is approximately 13.5 %, based on a monotonic test at 500 °C [50]. Using Equations (14) and (15), this results in a predicted multiaxial failure strain for this T-joint of 7.35 % and a predicted number of cycles to failure of approximately 3500 cycles. Assuming three temperature-pressure fluctuation cycles per day (which is an extreme case also), this corresponds to predicted failure after 3.2 years.

6. Concluding discussion

A multi-material PM, WM and CW finite element analysis method coupled with a non-linear kinematic and isotropic hardening cyclic plasticity model has been calibrated and validated against uniaxial high temperature low cycle fatigue testing of P91 steel and applied to the analysis of a P91 welded branch header T-joint connection. The results highlight the importance of incorporating multi-material cyclic plasticity parameters for prediction of plasticity and stress evolution in such welded connections. Some key conclusions are as follows:

- Identification and calibration of constitutive behavior parameters of PM, WM and HAZ from uniaxial cyclic experimental tests of P91 at 500 °C has facilitated new insight into the evolutions of uniaxial cross-weld tests.

- Detailed analyses of uniaxial cross weld specimens illustrate the complex stresses and strains in the vicinity of the heat affected zone. The heat affected zone is shown to play a critical role in the evolution of plastic strain and localised stresses. The evolution in the predicted stress distributions and stress-strain responses between the first cycle and those in the latter stages of the cyclic response are significantly different.

- The modelling results show that the plastic strain concentrates at the interface of PM-HAZ. This result is in agreement with the HTLCF experimental tests, where failure in the Type IV cracking region was observed [25,33].

- Plasticity was predicted to occur at the region of weldolet-header HAZ in a P91 welded branch header T-joint under isothermal conditions leading to elastic shakedown. The predicted critical location, due to a combined concentration of maximum tensile principal stress and HAZ plastic strain, corresponds to a location of observed premature cracking for in-service conditions.

- In-phase, fluctuating ±20 ^{o}C temperature variation with a mean value of 500 ^{o}C, with a significant increase in operating pressure and an assumed extreme system constraint on the branch end, was predicted to lead to cyclic plasticity and ratchetting in the weldolet-branch and weldolet-header HAZ at the inner crotch position. A strain-based failure model, with triaxiality effects included for multiaxial failure strain, was adopted to estimate failure life for the T-joint.

- The HAZ is a small-size region (2~3mm) and exhibits heterogeneities of micro-structure due to thermal gradients during welding, leading to differences in the mechanical properties compared to the PM and WM. Therefore, it is important to characterize the mechanical properties of welded joints with respect to PM, WM and HAZ materials, simultaneously. Some small-scale test methods have previously been proposed for non-cyclic behaviour of P91 HAZ material, e.g. Hyde *et al.* [51,52,53]. Touboul *et al.* [54] have presented digital image correlation (DIC) tests to characterize elastic-plastic (including isotropic and kinematic hardening) behaviour of the PM, WM and CG-HAZ, FG-HAZ and IC-HAZ regions of a welded P91 joints under (monotonic) tensile loading. A key challenge for future work is the development of a small-scale (e.g. micro-) fatigue test for the HAZ region and sub-regions.

- The present work is a first step towards the development of a design tool for next generation power plant weldments under cyclic deformation. The effects of creep and rate-dependent viscoplasticity are not considered in the present study. The creep-fatigue analysis of multi-material weldments will require the development of a combined creep-fatigue failure prediction methodology, incorporating the complex interactions of the cyclic softening with kinematic hardening effects, as presented here, while also including time-dependent creep stress re-distribution [13,14].

- Due to the hierarchical microstructure of 9Cr steels, the development of a microstructure-sensitive creep-fatigue constitutive and failure prediction modelling capability also represents a key next step to the successful suppression of Type IV cracking of 9Cr welded connections. The development of such a model would enable material degradation, such as low-angle boundary dislocation annihilation and martensitic lath to subgrain transformation, under CF deformation to be simulated from a physical basis.

Acknowledgements

This publication has emanated from research conducted with the financial support of Science Foundation Ireland under Grant SFI/2010/IN.1/I3015. The modeling work was supported by

the Irish Center for High-End Computing (ICHEC). The Authors also acknowledge the contributions made by the collaborators in this project, including Mr David Joyce and Dr Dongfeng Li (formerly NUI Galway), Prof. N.P. O'Dowd, Dr. P. Tiernan, and Mr. B.J. Golden of the University of Limerick and Prof. T.H. Hyde, Prof. W. Sun and Dr C. J. Hyde of the University of Nottingham.

References

1. T.P. Farragher, S. Scully, N.P. O'Dowd, S.B. Leen, Thermomechanical analysis of a pressurized pipe under plant conditions, *Transactions of the ASME Journal of Pressure Vessel Technology*, 135 (2013) 011204.
2. M. Sauzay, H. Brillet, I. Monnet, M. Mottot, F. Barcelo, B. Fournier, A. Pineau, Cyclically induced softening due to low-angle boundary annihilation in a martensitic steel. *Materials Science and Engineering A*, 400-401 (2005) 241-244.
3. M. Sauzay, B. Fournier, M. Mottot, A. Pineau, I. Monnet, Cyclic softening of martensitic steels at high temperature – Experiments and physically based modelling. *Materials Science and Engineering A*, 483-484 (2008) 410-414.
4. X. Hu, L. Huang, W. Yan, W. Wang, W. Sha, Y. Shan, K. Yang, Low cycle fatigue properties of CLAM steel at 823 K. *Materials Science and Engineering A*, 613 (2014) 404-413.
5. T.P., Farragher, S. Scully, N.P. O'Dowd, S.B. Leen, Development of life assessment procedures for power plant headers operated under flexible loading scenarios, International Journal of Fatigue, 49 (2013) 50-61.
6. F. Abe, M. Tabuchi, M. Kondo, S. Tsukamoto, Suppression of Type IV fracture and improvement of creep strength of 9Cr steel welded joints by boron addition. International Journal of Pressure Vessels and Piping, 84 (2007) 44-52.
7. H. Hongo, M. Tabuchi, T. Watanabe, Type IV creep damage behaviour in Gr.91 steel welded joints. *Metallurgical and Materials Transactions A*, 43 (2012) 1163-1173.
8. Y. Takahashi, M. Tabuchi, Evaluation of creep strength reduction factors for welded joints of Grade 122 steel, Journal of Pressure Vessel Technology, 133 (2011) 021401.
9. D.W.J. Tanner, W. Sun, T.H. Hyde, Cross-weld creep comparison of power plant steels CrMoV, P91 and P92, Journal of Pressure Vessel Technology, 135 (2013) 021408.
10. T.H. Hyde, W. Sun, Determining high temperature properties of weld materials, Int. Conf. on Advanced Technology in Experimental Mechanics, 1999.
11. T.H. Hyde, W. Sun, A. Tang, P.J. Budden, An inductive procedure for determining the stresses in multi-material components under steady-state creep, J Strain Analysis, 35(5) (2000) 347-357.
12. T.H. Hyde, W. Sun, A.A. Becker, Failure prediction for multi-material creep test specimens using a steady-state rupture stress approach, Int J Mech Sci, 42 (2000) 401-423.
13. W. Sun, T.H. Hyde, A.A. Becker, J.A. Williams, Comparison of the creep and damage failure prediction of the new, service-aged and repaired thick-walled circumferential CrMoV pipe welds using material properties at 640oC, International Journal of Pressure Vessels and Piping, 77 (2000) 389-398.
14. T.H. Hyde, A.A. Becker, W. Sun, J.A. Williams, Finite-element creep damage analyses of P91 pipes, International Journal of Pressure Vessels and Piping, 83 (2006) 853-863.
15. T.H. Hyde, A.A. Becker, W. Sun, A. Yaghi, J.A. Williams, S. Concari, Determination of creep properties for P91 weldment materials at 625 °C, 5th Int Conf on Mechanics and Materials in Design, 2006.

16. T.H. Hyde, W. Sun, Creep failure behaviour of a circumferential P91 pipe weldment with an anisotropic weld metal subjected to internal pressure and end load, Proc I Mech E, Part L, J Materials: Design and Applications, 220, (2006) 147-162.
17. S. Peravali, T.H. Hyde, K.A. Cliffe, S.B. Leen, "An anisotropic creep damage model for anisotropic weld metal," Trans ASME, J Pressure Vessel Technology, 131(2) (2009) 021401.
18. G. Rayner, T.H. Hyde, TH, S.B. Leen, W. Sun, Parametric analysis of stresses in welded branched pipes under creep conditions, Proc Instn Mech. Engrs, Part L: J. Materials Design & Applications, 219(L4), (2005), 231-248.
19. I.J. Perrin, D.R. Hayhurst, Creep constitutive equations for a 0.5Cr-0.5Mo-0.25V ferritic steel in the temperature range 600-675 °C. Journal of Strain Analysis, 31 (1996) 299-314.
20. D.R. Hayhurst, I.W. Goodall, R.J. Hayhurst, D.W.Dean, Lifetime prediction for high-temperature low-alloy ferritic steel weldments, J Strain Analysis, 40(7) (2012), 675-701.
21. C.R. Das, S.K. Albert, A.K. Bhaduri, G. Srinivasan, B.S. Murty, Effect of prior microstructure on microstructure and mechanical properties of modified 9Cr-1Mo steel weld joints. Mater. Sci. Eng. A., 477 (2008) 185-192.
22. S.L. Mannan, M. Valsan, High-temperature low cycle fatigue, creep-fatigue and thermomechanical fatigue of steels and their welds, Int. J. Mech. Sci., 48 (2006) 160-175.
23. R.D. Patel, Creep life assessment of welded trunnion and branch components using the R5 procedure, Int J Press Vessels and Piping, 80 (2003) 695-704.
24. R. Sandhya, R. Kannan, V. Ganesan, M. Valsan, K. Bhanu Sankara Rao, Low cycle fatigue properties of modified 9Cr-1Mo ferritic martensitic steel weld joints in sodium environment, Trans. Indian Institute Metals, 63 (2010) 553-557.
25. V. Shankar, M. Valsan, K. Bhanu Sankara Rao, S.D. Pathak, Low cycle fatigue and creep-fatigue interaction behaviour of modified 9Cr-1Mo ferritic steel and its weld joint, Trans Indian Institute Metals, 63 (2010) 622-628.
26. V. Shankar, R. Sandhya, M.D. Mathew, Creep-fatigue-oxidation interaction in Grade 91 steel weld joints, Materials Science and Engineering A, 528 (2011) 8428-8437.
27. Y. Takahashi, Study on Type-IV damage prevention in high-temperature welded structures of next-generation reactor plants, Part I: Fatigue and creep-fatigue behaviour of welded joints of modified 9Cr-1Mo steel, ASME PVP Conference, Canada, 2006.
28. H.C. Yang, Y. Tu, M.M. Yu, J. Zhao, Investigation of the low-cycle fatigue and fatigue crack growth behaviour of P91 base and weld joints, Acta Metallurgica Sinica (English letters), 17(4) (2004) 597-600.
29. B. Fournier, M. Sauzay, C. Caës, M. Noblecout, M. Mottot, A. Bougault, V. Rabeau, A. Pineau, "Creep-Fatigue-Oxidation Interactions in a 9Cr- 1Mo Martensitic Steel. Part I: Effect of Tensile Holding Period on Fatigue Lifetime," Int. J. Fatigue, 30 (2008) 649–662.
30. J. Okrajni, G. Junak, A. Marek, Modelling of the Deformation Process Under Thermo-Mechanical Fatigue Conditions, Int. J. Fatigue, 30 (2008) 324–329.
31. P. Matheron, G. Aiello, O. Ancelet, L. Forest, Recommendations for joint fatigue coefficients for welded P91 junctions at 550°C, Journal of Nuclear Materials, doi:10.1016/j.jnucmat.2015.07.016.
32. Yazid Madi, Naman Recho, Philippe Matheron, Low-cycle fatigue of welded joints: coupled initiation propagation model, Nuclear Engineering and Design 228 (2004) 179–194.

33. T.P. Farragher, S. Scully, N.P. O'Dowd, C.J. Hyde, S.B. Leen, High temperature, low cycle fatigue characterisation of P91 weld and heat affected zone material, Journal of Pressure Vessel Technology, 136 (2014) 021403.
34. A.A. Saad, C.J. Hyde, W. Sun, T.H. Hyde, "Thermal-Mechanical Fatigue Simulation of a P91 Steel in a Temperature Range of 400–600°C," ASME PVP Conference (2010).
35. J.-H. Lee, G.-H. Koo, Investigation of Ratcheting Characteristics of Modified 9Cr-1Mo Steel by Using the Chaboche Constitutive Model, Int. J. Pressure Vessels Piping, 84 (2007) 284–292.
36. R.A. Barrett, P.E. O'Donoghue, S.B. Leen. A dislocation-based model for high temperature cyclic viscoplasticity of 9-12Cr steels. Computational Materials Science, 92 (2014) 286-297.
37. R.A. Barrett, E. O'Hara, P.E. O'Donoghue, S.B. Leen, High temperature low cycle fatigue behaviour of MarBN at 600 °C. Transactions of the ASME Journal of Pressure Vessel Technology (2015) In-Press.
38. R.A. Barrett, P.E. O'Donoghue, S.B. Leen, An improved unified viscoplastic constitutive model for strain-rate sensitivity in high temperature fatigue, International Journal of Fatigue, 48 (2013) 192-204.
39. D.F. Li, B.J. Golden, N.P. ODowd, Multiscale modelling of mechanical response in a martensitic steel: A micromechanical and length-scale-dependent framework for precipitate hardening. Acta Mater., 80 (2014). 445-456.
40. G.-H. Koo, J.-H. Kwon, Identification of inelastic material parameters for modified 9Cr-1Mo steel applicable to the plastic and viscoplastic constitutive equations. International Journal of Pressure Vessels and Piping, 88 (2011), pp. 26-33.
41. A.S. Khan, S. Huang, Continuum Theory of Plasticity. John Wiley & Sons Inc, New York (1995).
42. J.L. Chaboche, G. Rousselier, On the plastic and viscoplastic constitutive equations – part I: rules developed with internal variable concept. Transactions of the ASME Journal of Pressure Vessel Technology, 105 (1983), pp. 153-158.
43. J.L. Chaboche, G. Rousselier, On the plastic and viscoplastic constitutive equations – part II: Application of internal variable concepts to the 316 stainless steel. Transactions of the ASME Journal of Pressure Vessel Technology, 105 (1983), pp. 159-164.
44. C.J. Hyde, W. Sun, S.B. Leen, "Cyclic thermo-mechanical material modelling and testing of 316 stainless steel", Int J Pressure Vessels and Piping, 87 (2010) 365-372.
45. R.A. Barrett, T.P. Farragher, C.J. Hyde, N.P. O'Dowd, P.E. O'Donoghue, S.B. Leen, A Unified Viscoplastic Model for High Temperature Low Cycle Fatigue of Service-Aged P91 Steel, Journal of Pressure Vessel Technology, 136 (2014) 021402.
46. J. Lemaitre, J. Chaboche, Mechanics of Solid Materials, Cambridge University Press, UK (1990).
47. Zhan, Z. A study of creep-fatigue interaction in a new Nickel-based superalloy. Ph.D. Thesis, University of Portsmouth, UK (2004).
48. C.A. Sweeney, B. O'Brien, F.P.E. Dunne, P.E. McHugh, S.B. Leen, Strain-gradient modelling of grain size effects on fatigue of CoCr stents, Acta Materialia, 78 (2014), 341–353.
49. M. Yatomi, A.D. Bettinson, N.P. O'Dowd, K.M. Nikbin, Modelling of damage development and failure in notched-bar multi-axial creep tests, Fatigue Fract Eng Mats Structs, 27 (2004), 283-295.
50. B.J. Golden, D.F. Li, P. Tiernan, S. Scully, N.P. O'Dowd, Deformation characteristics of a high chromium power plant steel at elevated temperatures. Proceedings of the

2015 ASME Pressure Vessels and Piping Conference, July 19-23, 2015, Boston, USA.
51. T.H. Hyde, W. Sun, Determining High Temperature Properties of Weld Materials, J. Strain Analysis, 43 (2000) 408-414.
52. T. H. Hyde, B. S M Ali, W. Sun, Interpretation of small ring creep test data, J. Strain Analysis, 48 (2013) 269-278.
53. D. W. J. Tanner, M. Saber, W. Sun, T. H. Hyde, Creep Behavior of P92 and P92 Welds at 675 °C, Journal of Pressure Vessel Technology, 135 (2013), 051404.
54. M. Touboul, J. Crepin, G. Rousselier, F. Latourte, S. Leclercq, Identification of Local Viscoplastic Properties in P91 Welds from Full Field Measurements at Room Temperature and 625 °C. Experimental Mechanics, 53 (2013),455–468.

Figures

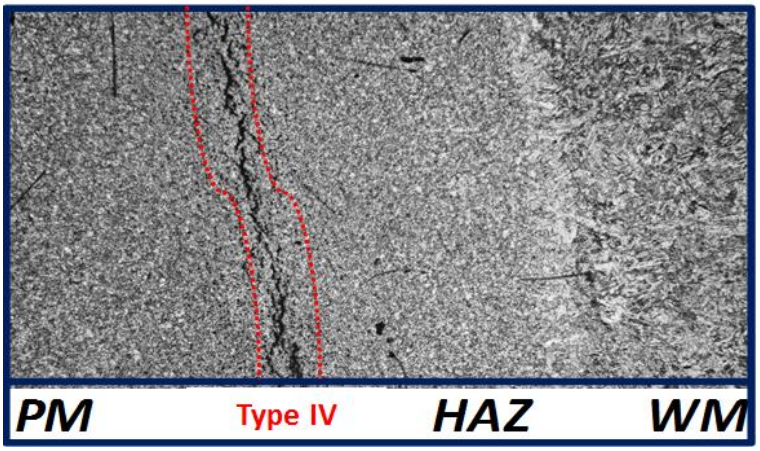

Figure 1: SEM image of Type IV cracking in the HAZ of an in-service P91 steel T-joint.

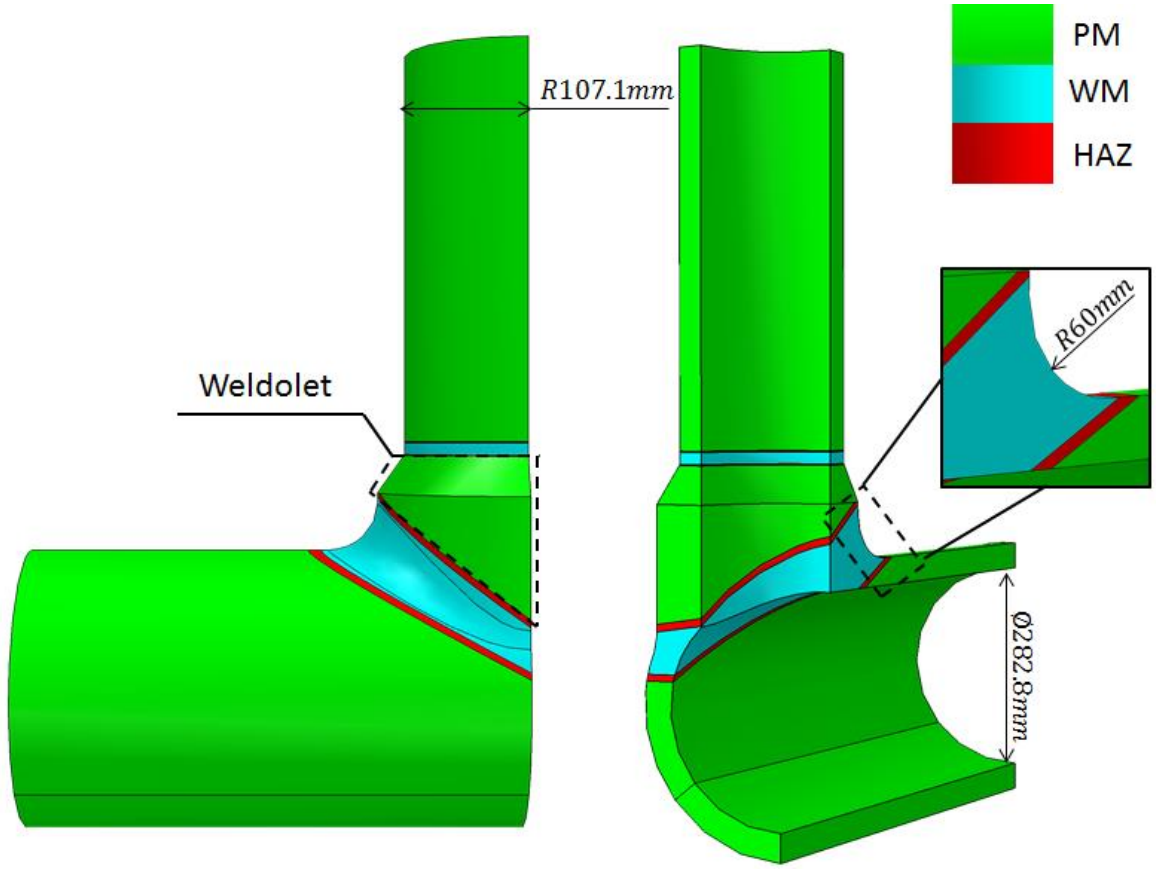

Figure 2: Image of the T-Joint showing the PM, WM and HAZ for branch weldolet and weldolet-header connections.

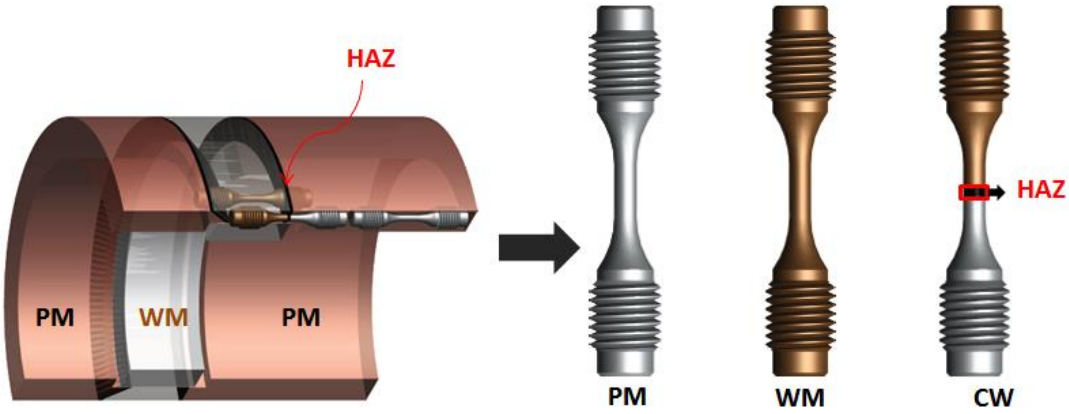

Figure 3: Positions of different HTLCF test specimens, showing PM, WM and CW (inclusive of HAZ) specimens.

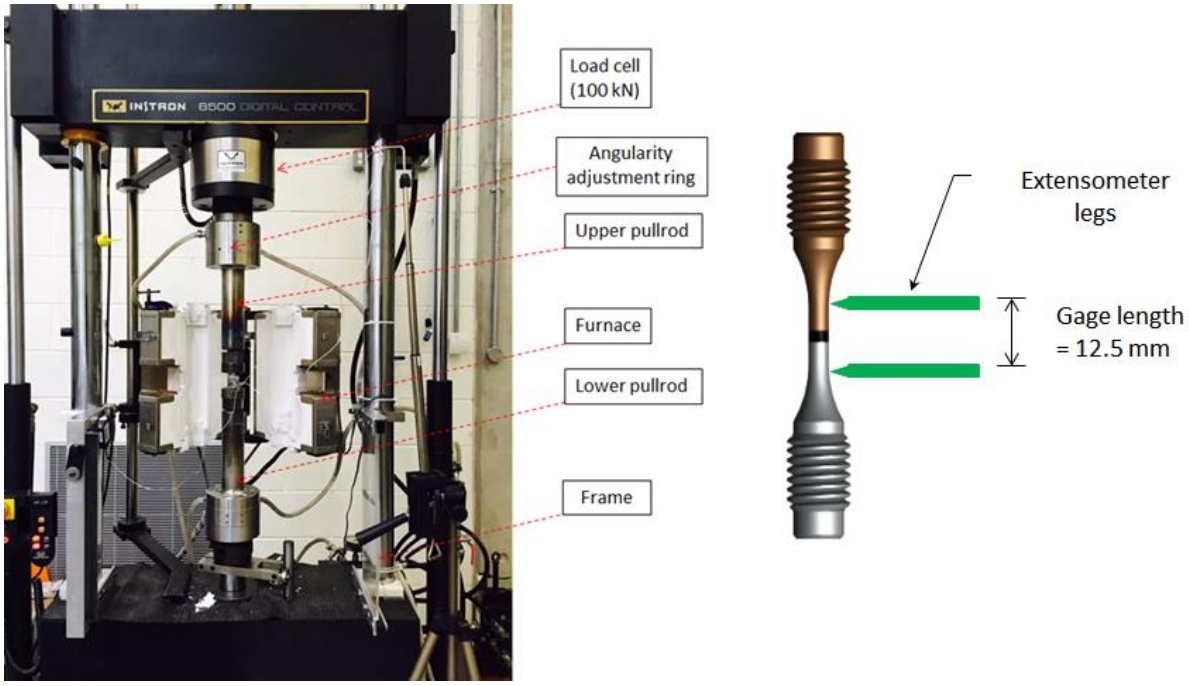

Figure 4: (a) Photograph of the INSTRON 8800 HTLCF test rig at NUI Galway and (b) setup and location of the extensometer in relation to the CW specimen.

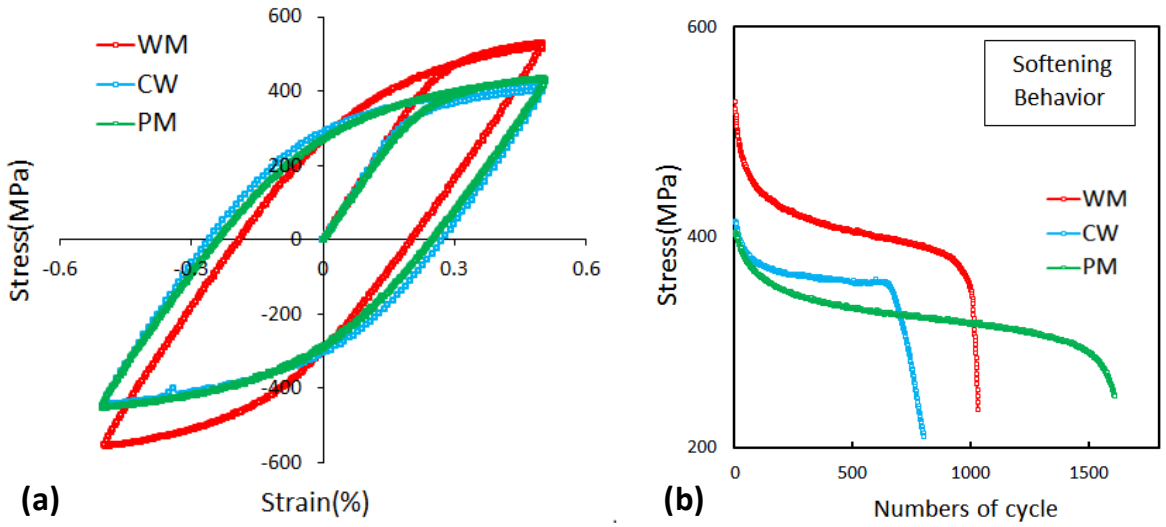

Figure 5: Measured results of the (a) stress-strain response for the initial cycle and (b) cyclic evolution of maximum stress for PM, WM and CW material for an applied strain-range of 1.0 % and applied strain-rate of 0.0333 %/s at 500 °C.

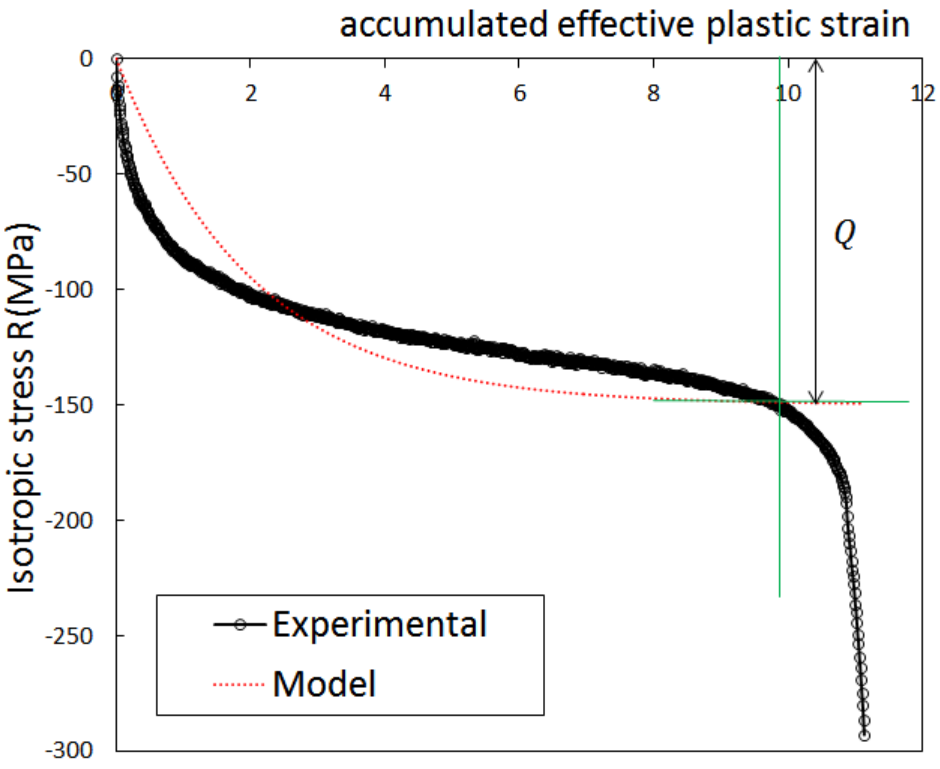

Figure 6: Identification of the cyclic softening material parameters (Q, b) for the WM.

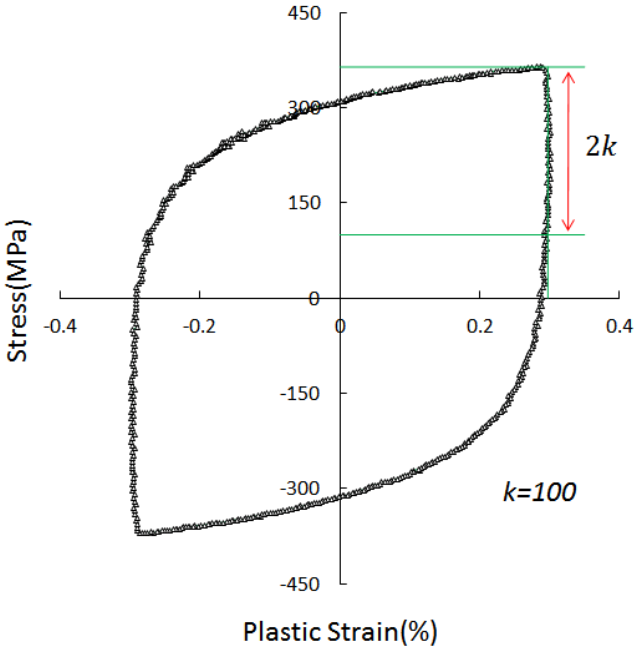

Figure 7: Identification of the initial cyclic yield stress, k, for the PM.

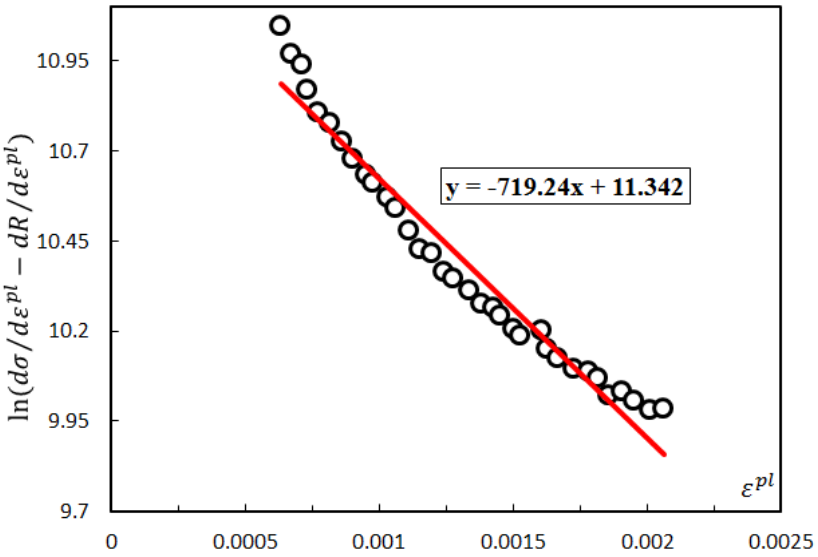

(a)

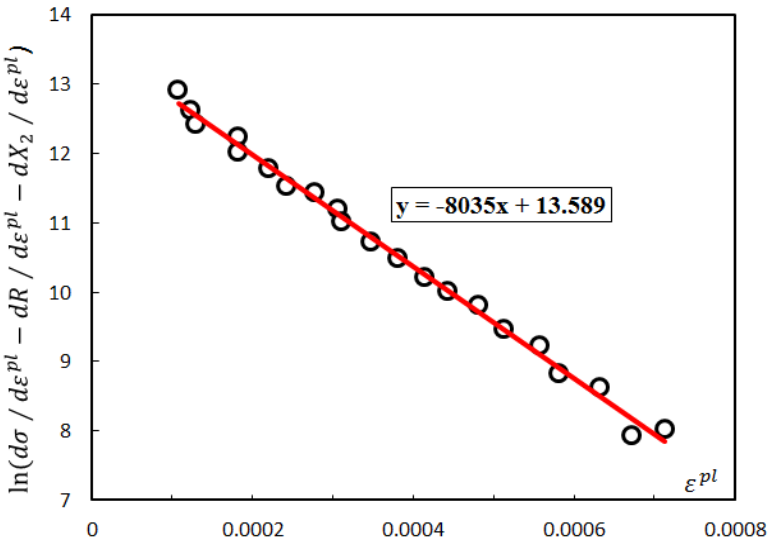

(b)

Figure 8: Identification of the NLKH parameters (a) C_2 and γ_2 and (b) C_1 and γ_1 for the WM.

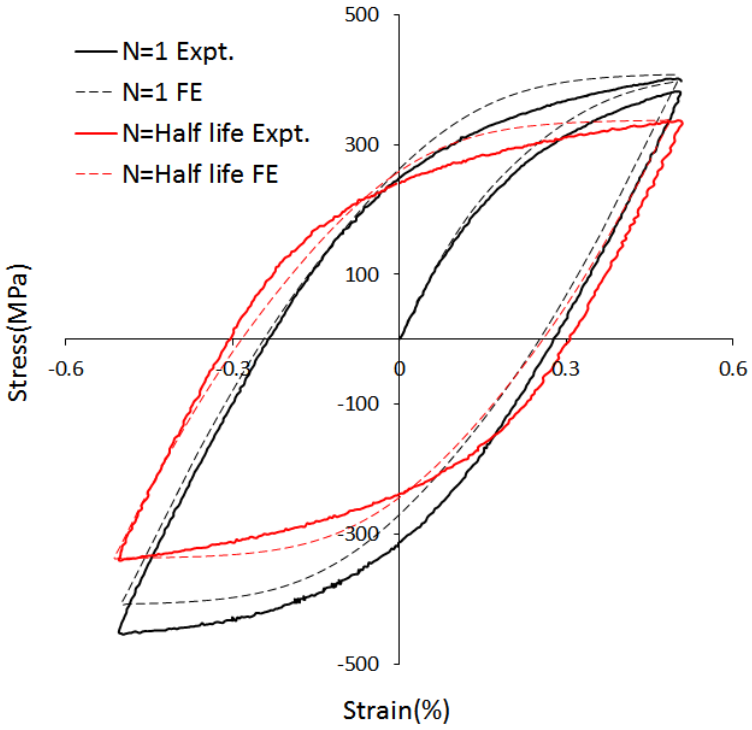

(a)

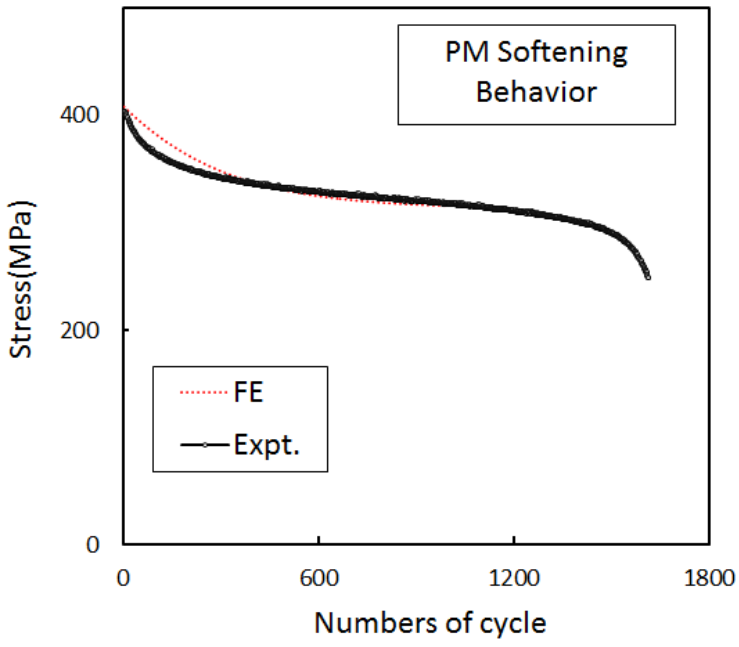

(b)

Figure 9: Comparison of the model predicted and experimentally measured (a) stress-strain response and (b) evolution of cyclic softening in the PM for an applied strain-range of 1.0 % at 500 °C.

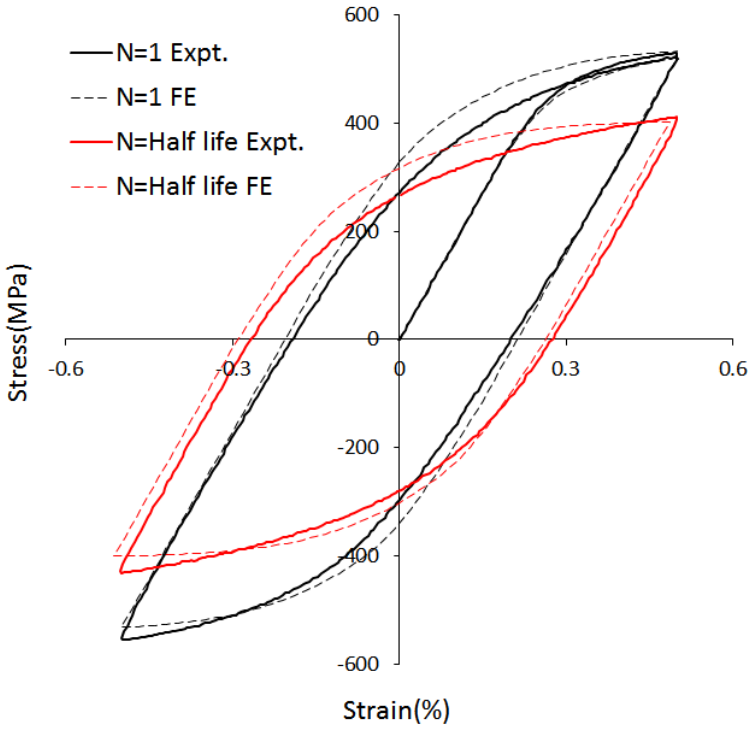

(a)

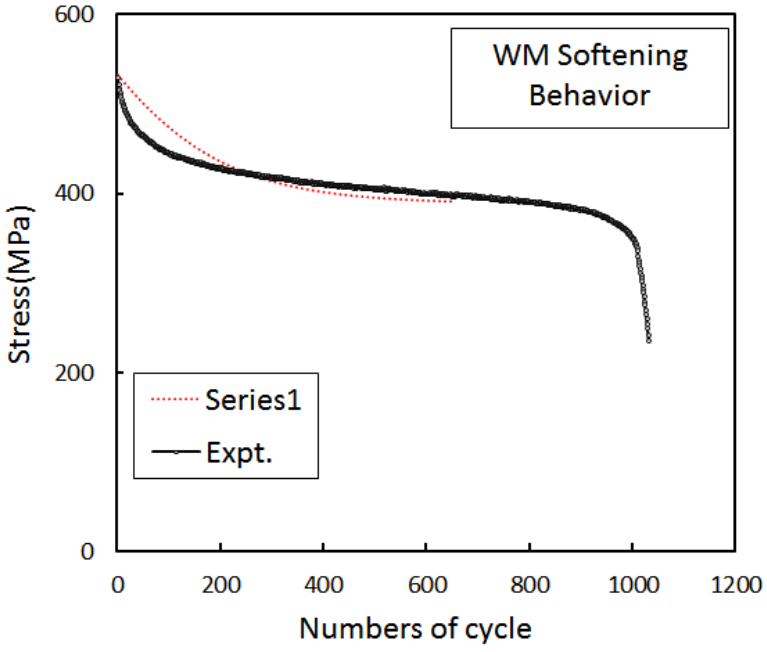

(b)

Figure 10: Comparison of the model predicted and experimentally measured (a) stress-strain response and (b) evolution of cyclic softening in the WM for an applied strain-range of 1.0 % at 500 °C.

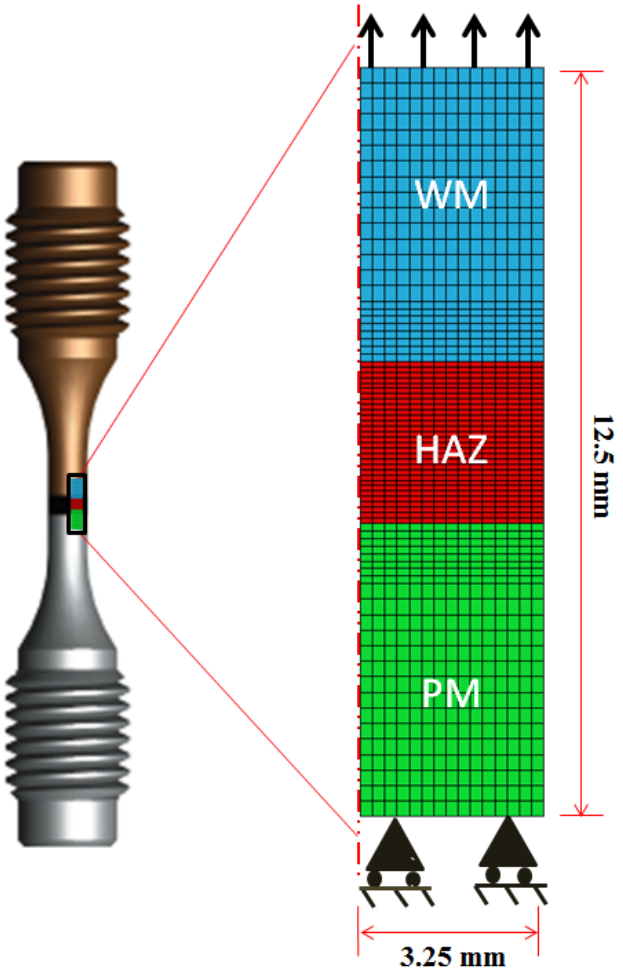

Figure 11: Schematic representation of the three-material model of the CW specimen gauge length.

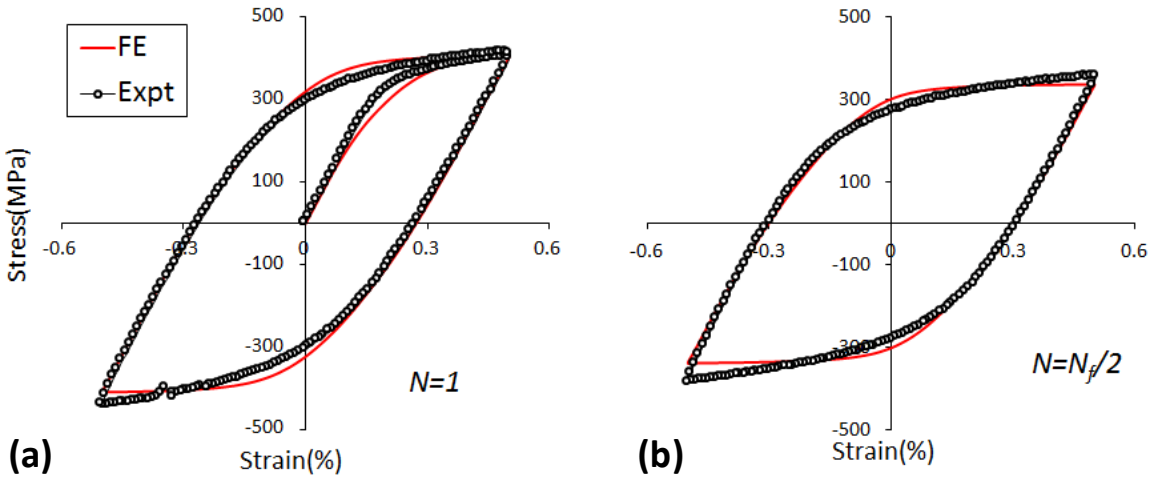

Figure 12: Typical correlation of the predicted and measured evolution of CW stress-strain response for (a) the initial cycle and (b) the half-life cycle for an applied strain-range of 1.0 % and strain-rate of 0.0333 %/s at 500 °C.

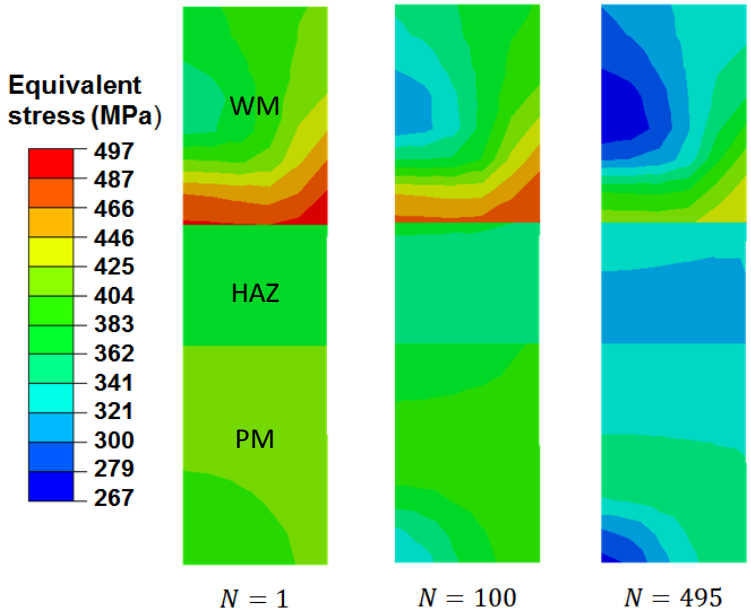

Figure 13: Evolution of von Mises stress in the FE model of the CW specimen, for a 1.0 % strain-range for (a) the initial cycle, (b) 100th cycle and (c) half-life at 500 °C.

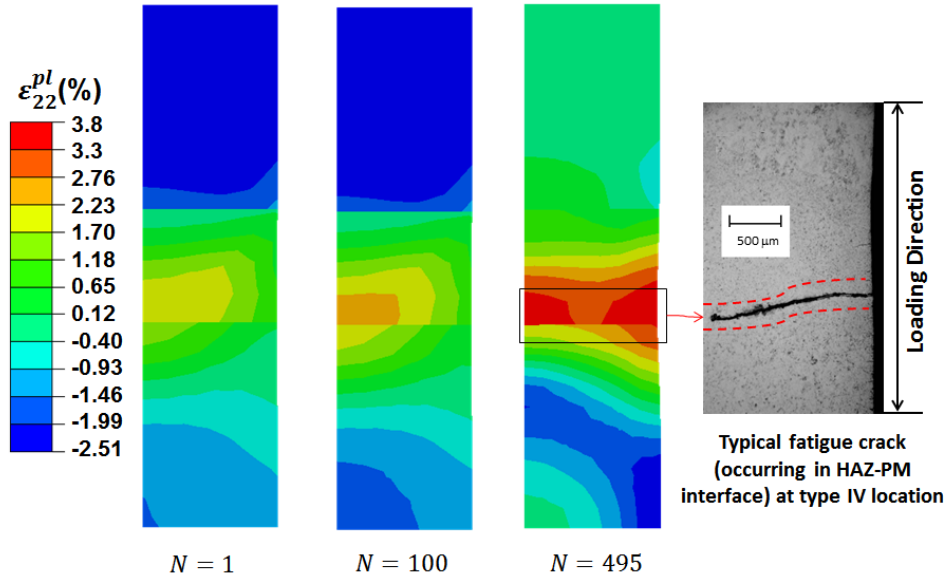

Figure 14: Evolution of (axial) plastic strain distribution in the FE model of the CW specimen, for a 1.0 % strain-range for (a) the initial cycle, (b) 100th cycle and (c) half-life at 500 °C.

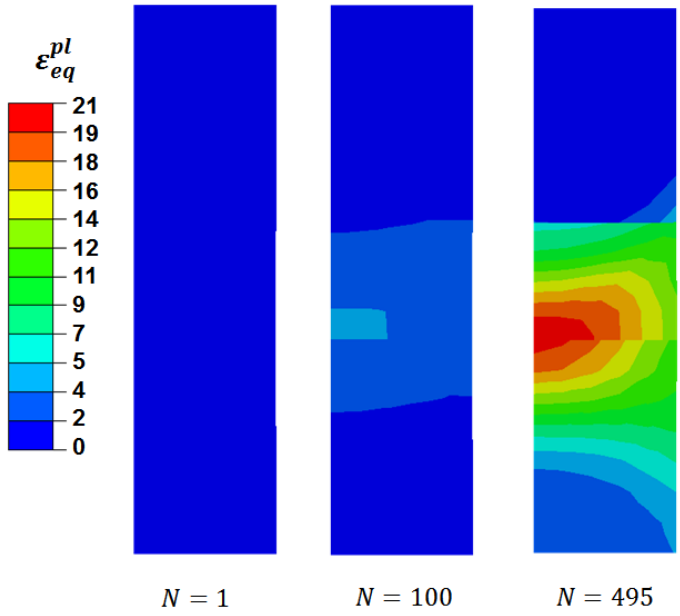

Figure 15: Evolution of equivalent plastic-strain distribution in the FE model of the CW specimen, for a 1.0 % strain-range for (a) the initial cycle, (b) 100th cycle and (c) half-life at 500 °C.

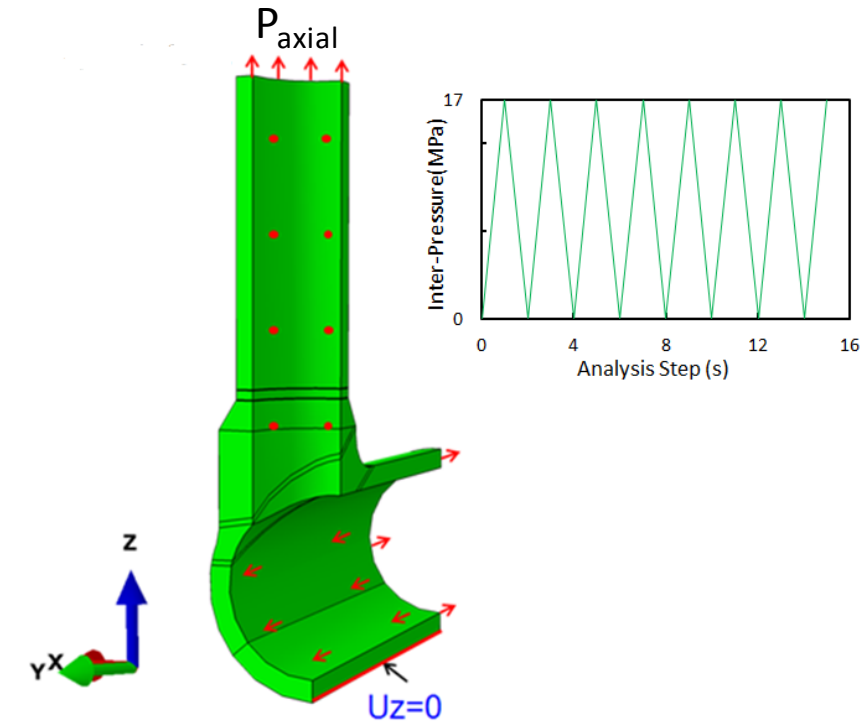

(a)

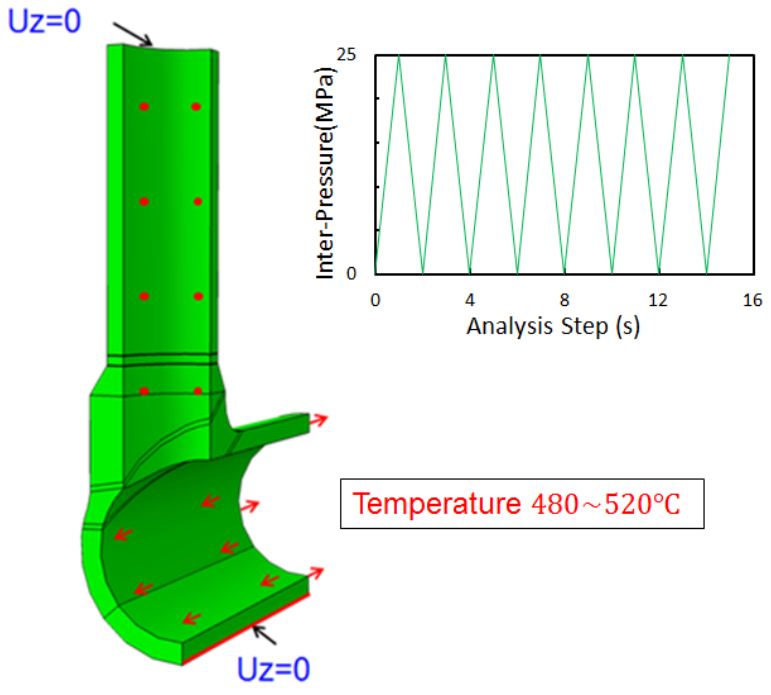

(b)

Figure 16: Loading and boundary conditions on the T-joint FE model for (a) case 1 and (b) case 2.

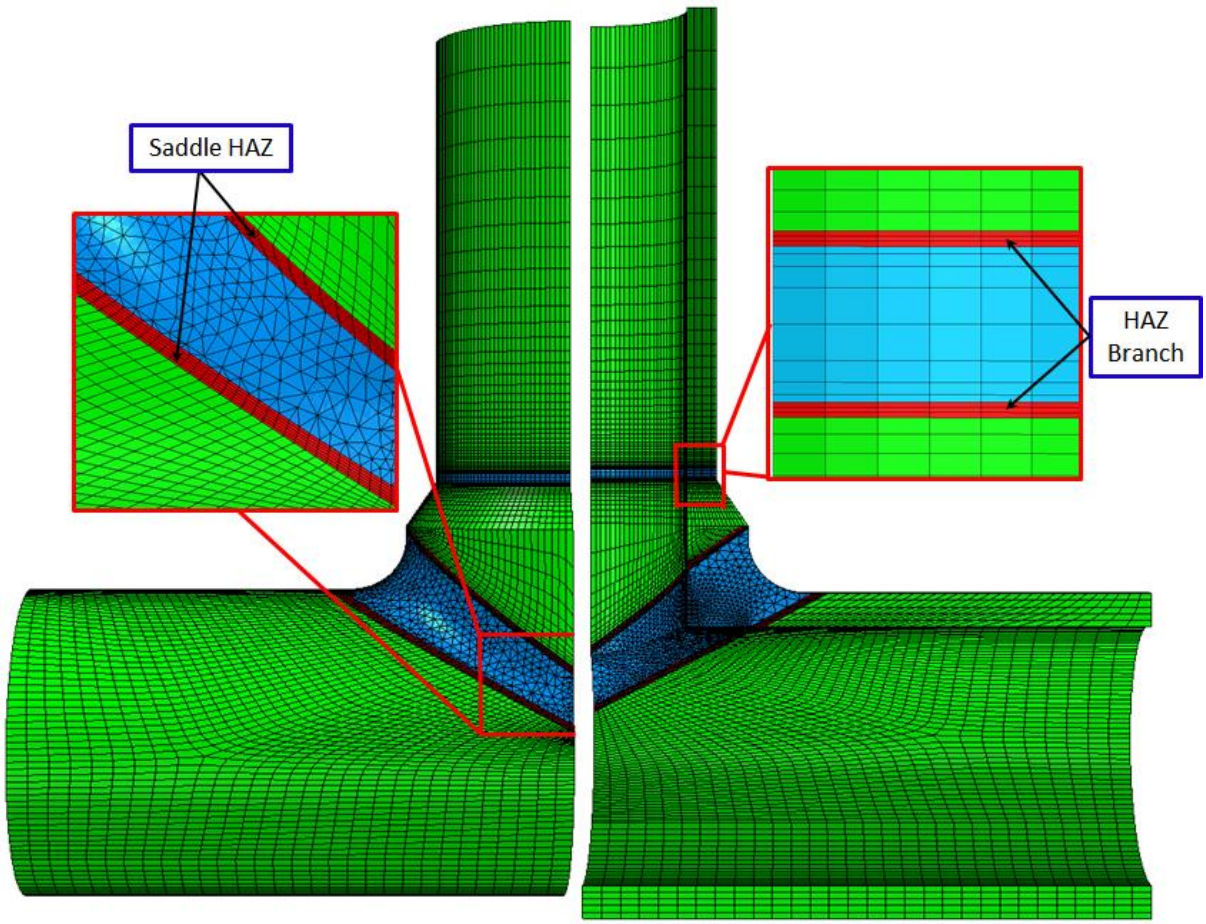

Figure 17: Details of mesh refinement for converged FE model of T-joint.

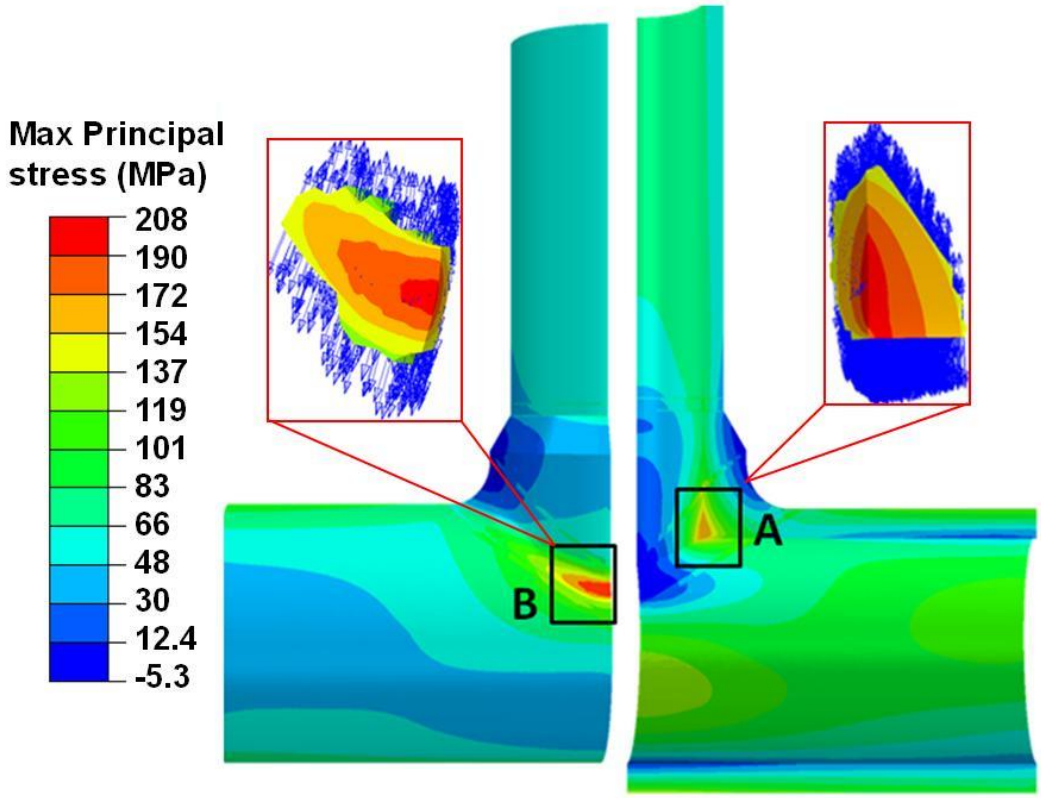

Figure 18: Contour plots of maximum principal stress distribution for the case 1 model of the T-joint. The two primary areas of interest are labelled A and B, with vectors indicating the direction of maximum principal stresses and possible tensile fatigue failure.

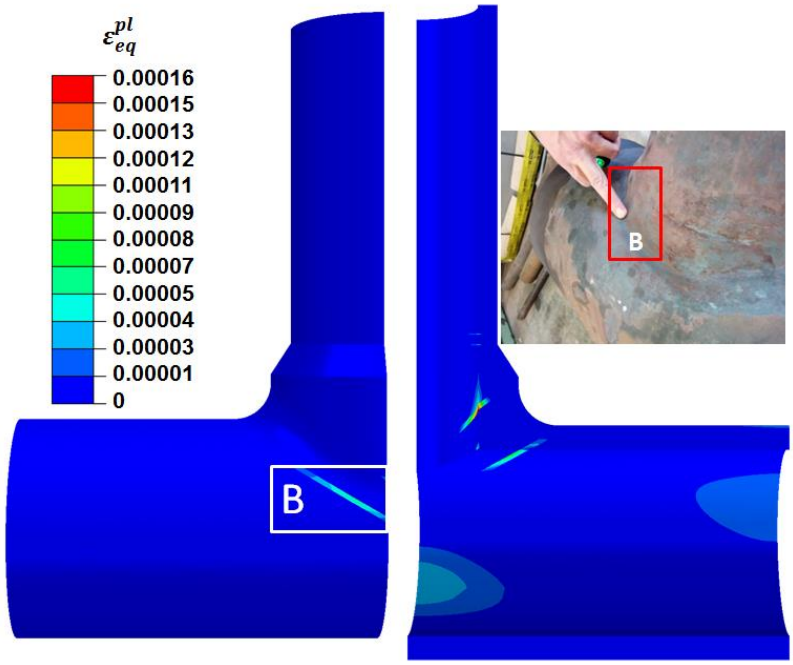

Figure 19: Contour plot of equivalent plastic strain in the T-joint model, showing a concentration in the weldolet-header HAZ at the inner bore crotch region for case 1 with an internal pressure of 25 MPa.

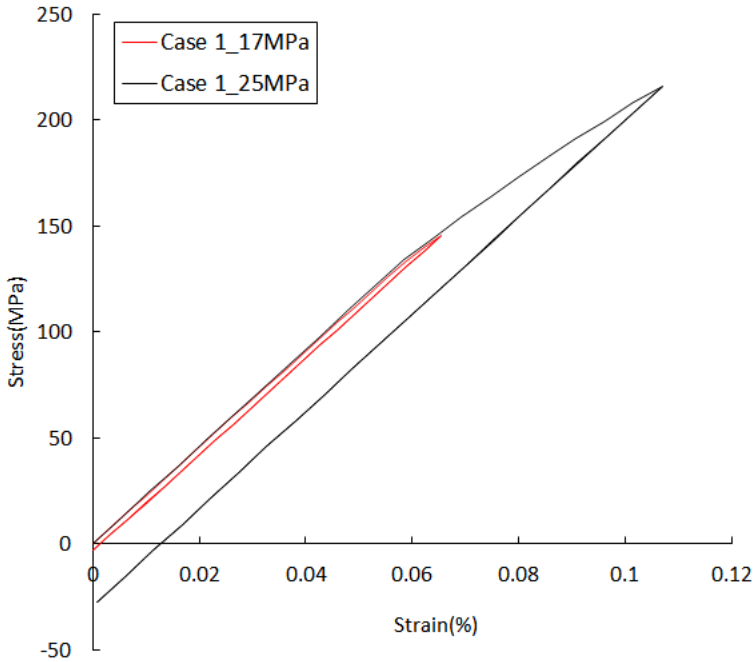

Figure 20: Predicted evolution of $\boldsymbol{\sigma_{11} - \varepsilon_{11}}$ response of the weldolet-header HAZ inner bore crotch region hot-spot (A), for 17 MPa and 25 MPa internal pressure load cases.

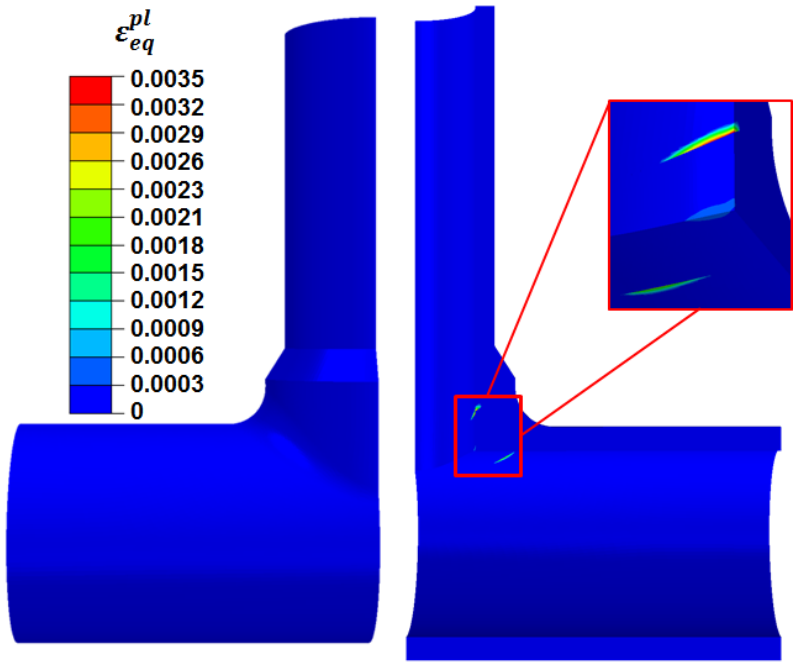

Figure 21: Contour plots of predicted equivalent plastic strain for the case 2 T-joint model after 51 cycles, showing a concentration in the weldolet-header HAZ at the inner bore crotch position for an internal pressure of 25 MPa.

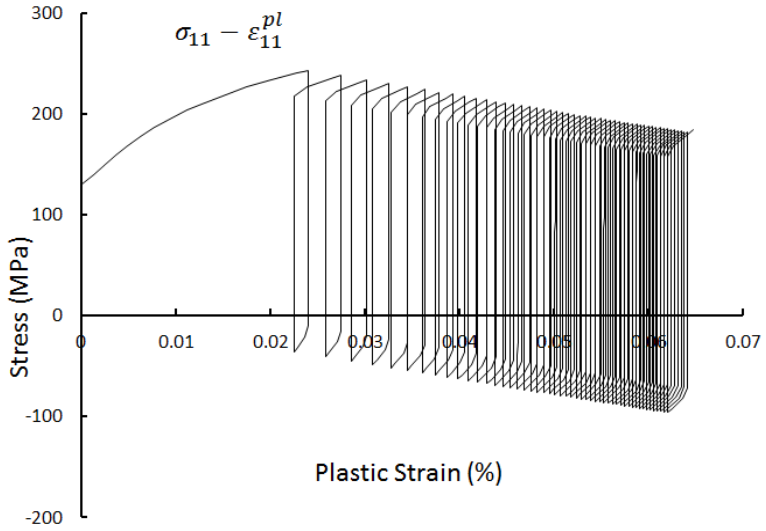

Figure 22: Predicted evolutions of hoop stress-plastic strain response of the weldolet-header HAZ at the inner bore crotch region hotspot, for case 2.

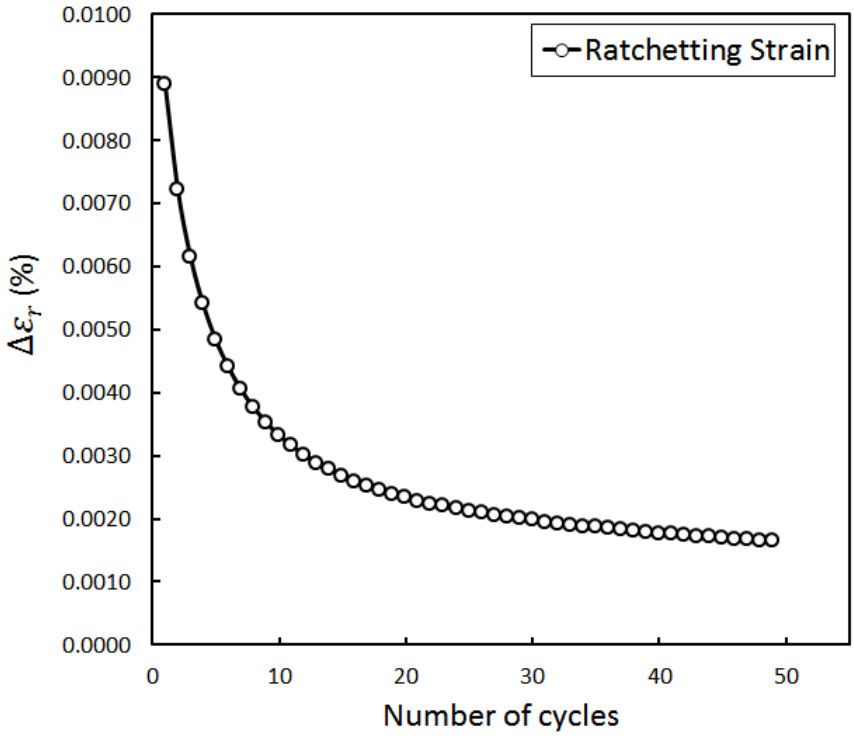

Figure 23: Multi-axial ratchetting strain evolution of weldolet-header HAZ at the inner bore crotch region hot-spot for case 2.

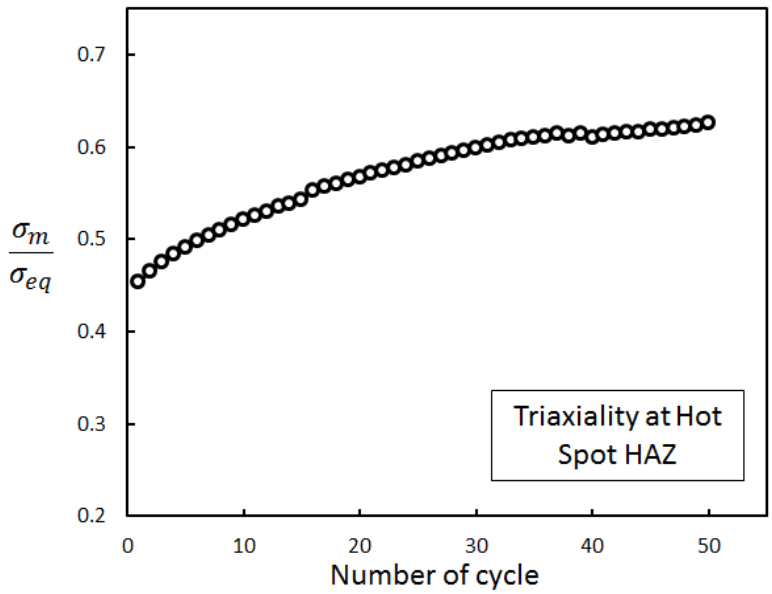

Figure 24: Predicted evolutions of triaxiality variation response in the weldolet-header HAZ at the inner bore crotch region hot-spot, for case 2.

Tables

Table 1: Identified cyclic plasticity material parameters for WM, PM and HAZ ex-service P91 steel at 500 °C.

Material	E (MPa)	k (MPa)	C_1 (MPa)	γ_1	C_2 (MPa)	γ_2	Q (MPa)	b
WM	181000	325	797311	8035	79567	719	-150	0.6
PM	170222	130	728687	12534	258073	1100	-96.5	0.25
HAZ	220000	120	763000	10284	168820	966	-80	0.1

Table 2: Key dimensions of the header-branch T-joint.

Pipe Section	Inner Radius (mm)	Thickness (mm)
Branch	107.1	29.4
Header	141.4	26.1
Branch weld	–	15
Branch HAZ	–	1.5
Fillet Weld radius	60	
Fillet Weld HAZ	–	7.2

Table 3: Summary of the results of the T-joint case study.

Thermal Condition	Pressure Load (MPa)	Branch End BC	Outcome
Isothermal 500 ºC	**17 (case 1)**	**Axial Pressure**	**Elastic Shakedown**
	25	Axial Pressure	Elastic Shakedown
	17	Axial Constrained	Elastic Shakedown
	25	Axial Constrained	Elastic Shakedown
480 ºC - 520 ºC, in-phase with cyclic pressure	17	Axial Pressure	Elastic Shakedown
	25	Axial Pressure	Elastic Shakedown
	17	Axial Constrained	Elastic Shakedown
	25 (case 2)	**Axial Constrained**	**Ratcheting**